Materials Today Energy 29 (2022) 101094

Contents lists available at ScienceDirect

Materials Today Energy

journal homepage: www.journals.elsevier.com/materials-today-energy/

Effect of atomic substitution on the sodium manganese ferrite thermochemical cycle for hydrogen production

Francesco Torre [a], Teresa Aguilar Sanchez [a], Stefania Doppiu [a, *], Mikel Oregui Bengoechea [b], Pedro Luis Arias Ergueta [b], Elena Palomo del Barrio [a, c]

[a] Centre for Cooperative Research on Alternative Energies (CIC energiGUNE), Basque Research and Technology Alliance (BRTA), Alava Technology Park, Albert Einstein 48, 01510 Vitoria-Gasteiz, Spain
[b] Universidad del Pais Vasco - Euskal Herriko Unibertsitatea, Escuela de Ingeniería, Plaza Torres Quevedo, 1, 48013 Bilbao, Spain
[c] Ikerbasque, Basque Foundation for Science, Bilbao 348013, Spain

ARTICLE INFO

Article history:
Received 8 April 2022
Received in revised form
6 July 2022
Accepted 7 July 2022
Available online 25 August 2022

Keywords:
Thermochemical water splitting
Sodium manganese ferrite cycle
Carbonation
Decarbonation
Fuel production
Cation substitution

ABSTRACT

This work presents the effect of atomic substitution on the $MnFe_2O_4$–Na_2CO_3 thermochemical cycle for H_2 production. The non-oxidative decarbonation/carbonation reaction of the $MnFe_2O_4$–Na_2CO_3 mixture is investigated as the starting reference. Repeated cycling results in a 30% loss of reversibility due to an overall reduction of the reactive interfaces. The substitution of Na_2CO_3 for Li_2CO_3 decreases the decarbonation onset temperature by about 100 °C, but almost no reversibility is observed during the cycles due to the irreversible Li^+ intercalation. The effect of partial Mn substitution for Ca, Ni, and Zn is presented. The 5% Zn mixture shows the best decarbonation/carbonation reversibility and is tested for H_2 production together with $MnFe_2O_4$–Na_2CO_3. The reference mixture produces more H_2 during the first cycle (≈1.1 vs. 0.7 mmol/g), but its production drastically drops by two orders of magnitude upon cycling and becomes negligible after 5 cycles. By contrast, the Zn-doped mixture exhibits a stable H_2 production of 0.22 mmol/g with no decreasing trend observed from cycle 2 to cycle 5. As result, in the fifth cycle, the Zn-doped mixture produces 23 times more H_2 than $MnFe_2O_4$–Na_2CO_3. Thermogravimetry and X-ray diffraction confirm that doping with Zn significantly improves the regeneration of the reactants.

1. Introduction

Thermochemical water splitting (WS) represents a very promising and elegant solution for sustainable large-scale hydrogen production [1–3]. This technology uses water and heat as input, to produce H_2 and O_2. Although direct water thermolysis can be achieved in principle, the extreme temperatures (T > 2200 °C) and the necessity to separate H_2 from O_2 make this solution impractical [4]. Improvements can be achieved by dividing the overall process into consecutive reactions (minimum two) that are cyclically repeated through a so-called thermochemical cycle [5]. This allows to lower the operating temperatures and produce H_2 and O_2 in separate steps, reducing the risk of accidents.

Among more than 300 proposed so far, two-step thermochemical cycles based on metal oxides (e.g. SnO_2, ZnO, CeO_2, Mn_3O_4, Fe_xO_y) rely on relatively low-cost materials and do not involve dangerous or corrosive reaction intermediates [6–12]. However, the regeneration (reduction) step typically requires temperatures >1500 °C, which negatively affects the long-term materials performances and poses significant challenges when choosing the materials for the thermochemical reactors [13]. The addition of secondary compounds has been proposed to lower the reaction temperatures below 1000 °C. In this regard, a recent assessment considering process economics, environmental impact, cyclability, and simplicity of operation highlighted the $MnFe_2O_4$–Na_2CO_3 cycle as one of the best for practical applications [14]. This cycle was initially proposed by Y. Tamamura et al. [15,16] and then further investigated by C. Alvani et al. [17–25]. Beyond lab-scale experiments, the feasibility of this thermochemical cycle has also been proven in a small solar concentration facility [25].

In first approximation, this thermochemical cycle consists of two steps [15] and can work at temperatures around 800–750 °C:

* Corresponding author.
E-mail address: sdoppiu@cicenergigune.com (S. Doppiu).

https://doi.org/10.1016/j.mtener.2022.101094

$$2MnFe_2O_4(s) + 3Na_2CO_3(s) + H_2O(g) \rightarrow 6NaFe_{2/3}Mn_{1/3}O_2(s) + H_2(g) + 3CO_2(g) \quad (1)$$

$$6NaFe_{2/3}Mn_{1/3}O_2(s) + 3CO_2(g) \rightarrow 2MnFe_2O_4(s) + 3Na_2CO_3(s) + 0.5O_2(g) \quad (2)$$

However, a more complex reaction path was experimentally observed, as it was clearly described by Varsano et al. [23]. In particular, the hydrogen production reaction (1) was shown to proceed through two separate steps. First, the non-oxidative partial decarbonation takes place, where 2/3 of Na_2CO_3 reacts with $MnFe_2O_4$. As a result of this reaction, CO_2 is released, and sodium intercalates in the cubic spinel phase to form a fine mixture of $NaFeO_2$ and MnO:

$$2MnFe_2O_4(s) + 3Na_2CO_3(s) \rightarrow 2(MnO{*}2NaFeO_2)(s) + Na_2CO_3(s) + 2CO_2(g) \quad (3)$$

The formation of the ($MnO{*}NaFeO_2$) compound paves the way to the subsequent reaction with H_2O steam to produce H_2 (4). Mn^{2+} is oxidized to Mn^{3+} to form $NaFe_{2/3}Mn_{2/3}O_2$, which has the same crystal structure as $NaFeO_2$. At this point, more Na^+ can be intercalated, which drives the decomposition of the remaining Na_2CO_3.

$$2(MgO{*}2NaFeO_2)(s) + Na_2CO_3(s) + H_2O(g) \rightarrow 6Na\left(Mn_{\frac{1}{3}}Fe_{\frac{2}{3}}\right)O_2(s) + 2CO_2(g) + H_2(g) \quad (4)$$

Once the WS reaction is completed, $NaFe_{2/3}Mn_{2/3}O_2$ is exposed to a CO_2-rich gas, which promotes the sodium oxide deintercalation to form Na_2CO_3. As result, the Na content in the $NaFe_{2/3}Mn_{2/3}O_2$ progressively decreases and the layered structure collapses. The reduction of Mn^{3+} to Mn^{2+} and the corresponding release of molecular oxygen eventually leads to the regeneration of $MnFe_2O_4$ and Na_2CO_3:

$$6NaFe_{2/3}Mn_{1/3}O_2(s) + 3CO_2(g) \rightarrow 2MnFe_2O_4(s) + 3Na_2CO_3(s) + \frac{1}{2}O_2(g) \quad (5)$$

Unfortunately, particle sintering and coalescence of a Na_2CO_3 layer tend to hinder the complete regeneration of the starting reactants, leading to a drastic decrease in the H_2 production upon prolonged cycling [24].

In general, the improvement of the reaction kinetics and reversibility, as well as the decrease of the operating temperatures, is highly important to increase the efficiency of thermochemical cycles, as well as to broaden their potential fields of application [26]. Speed up the reaction kinetics means increasing the H_2 production per unit of time, while long-term stability of the materials is fundamental for the overall process to be feasible and competitive. In this sense, lowering the operating temperature reduces the sintering of the used oxides and reduces the requirements for the materials needed to construct thermochemical reactors.

Atomic substitution, reduction of the crystallite size, and addition of inert compounds are common strategies to improve materials performances [7,27–35]. For instance, atomic substitution significantly improved the performances of CeO_2- and perovskites-based thermochemical cycles for fuel production [36–41]. A straightforward relation between cycle performances and the microstructural changes induced by atomic substitution was reported in some cases. The regeneration temperature of some doped perovskites decreased when introducing doping elements with lower atomic size. Such behavior was attributed to an increase in the atomic size mismatch that, in turn, led to a higher local disorder [38]. Concerning ferrite-carbonate cycles, investigations performed on single metal oxides (Mn_3O_4, Fe_3O_4, and Co_3O_4) and carbonates (Na_2CO_3, Li_2CO_3, and K_2CO_3) showed that the H_2 evolution rate was found to vary depending on the specific cation combinations [42].

To the best of our knowledge, similar approaches have not yet been reported for the $MnFe_2O_4$–Na_2CO_3 thermochemical cycle. Thus, the present work represents the first attempt in this direction. Particular attention is given to the non-oxidative decarbonation reaction (reaction 3) as it represents the first step of the overall thermochemical cycle. The decarbonation-carbonation reaction of $MnFe_2O_4$–Na_2CO_3 is followed during 10 consecutive cycles, and the related structural changes are investigated. The effect of atomic substitution is then explored by using $MnFe_2O_4$–Na_2CO_3 as the basis for comparison. Starting from the $MnFe_2O_4$–Na_2CO_3 system, the effect of atomic substitution on its reactivity is faced through two distinct approaches. Evaluating the substitution of Na for Li and K cations and partially substituting Mn^{2+} for Ca^{2+}, Ni^{2+}, and Zn^{2+}. In the latter case, ferrites with general formula $Mn_{1-x}A_xFe_2O_4$, with A being Ni, Zn, Ca, and x = 0.05, 0.10, and 0.50 are synthesized and tested through decarbonation/carbonation cycles together with Na_2CO_3. The most promising doped mixture is then tested for the H_2 production reaction, and its performances are compared with those of the reference $MnFe_2O_4$–Na_2CO_3 system.

2. Material and methods

2.1. Synthesis of Mn ferrite oxides

Manganese ferrite-based oxides, with spinel structure, were synthesized following the self-combustion method; glycine ($C_2H_5NO_2$, 98.5%, Sigma Aldrich) was used as complexant and fuel agent [43]. An aqueous solution of $Fe(NO_3)_3{\cdot}9H_2O$ (99%, Alfa Aesar) and $Mn(NO_3)_2{\cdot}4H_2O$ (99%, Alfa Aesar) was prepared; a molar ratio of 2:1 between Fe^{3+} and Mn^{2+} and a total cation concentration of 1 M were ensured. A 1 M solution of glycine was then added and the final solution was stirred for 2 h. The solution was transferred into a Petri-type dish and kept at 100 °C until a red-brownish gel was formed. Finally, the self-combustion reaction was carried out at 350 °C, where a black-brownish, foamy product was obtained.

The same methodology was used to synthesize modified manganese ferrites with general formula $Mn_{1-x}A_xFe_2O_4$, with A being Ni, Zn, Ca, and x = 0.05, 0.1, and 0.5. To this end, part of the Mn^{2+} precursor was substituted by the nitrate of the corresponding divalent dopant cation—i.e. $Zn(NO_3)_2{\cdot}6H_2O$ (98%, Alfa Aesar), $Ni(NO_3)_2{\cdot}6H_2O$ (EssentQ®, Scharlau), and $Ca(NO_3)_2{\cdot}4H_2O$ (99%, Sigma Aldrich). On the other side, the Fe^{3+} concentration was not changed. In this way, the ratio between the divalent and trivalent cations was maintained constant at 1:2. The atomic distribution of divalent and trivalent cations in the octahedral and tetrahedral sites of the spinel lattice can change depending on the specific chemical composition, the synthesis method, and the microstructural features [44,45]. The determination of the exact atomic distribution is not straightforward and will not be addressed in this work. In fact, the Mn substitution we refer to should be intended only in terms of chemical composition—i.e. the partial replacement of Mn^{2+} with Ca^{2+}, Ni^{2+}, and Zn^{2+}.

For the sake of simplicity, the different oxides will be indicated by referring to the percentage of Mn atomic substitution; for

instance, $Mn_{0.5}Ca_{0.5}Fe_2O_4$ will be referred to as 50 at.% Ca, $Mn_{0.95}Ni_{0.05}Fe_2O_4$ as 5 at.% Ni, etc. (see Table 1).

2.2. Thermal analysis

2.2.1. Non-oxidative decarbonation reaction of the $MnFe_2O_4$–Na_2CO_3 mixture

Temperature programmed desorption (TPD) experiments were performed to investigate the decarbonation/carbonation behavior of the different mixtures of spinel ferrites and carbonates. For each experiment, the selected spinel ferrite and carbonate were mixed at a 1:1 M ratio using a mortar. The choice of this stoichiometry can be understood by looking at the non-oxidative decarbonation step described by Eq. (3). In non-oxidizing conditions (absence of H_2O), only 2/3 of the Na_2CO_3 reacts with $MnFe_2O_4$, while the remaining 1/3 of Na_2CO_3 does not participate in the reaction. This corresponds to a $MnFe_2O_4$: Na_2CO_3 molar ratio of 1:1. About 15–20 mg of the mixture were transferred to an alumina crucible and located in a NETZSCH STA 449 F3 thermobalance. Preliminary isothermal experiments were performed on the $MnFe_2O_4$–Na_2CO_3 mixture at 600, 700, 750, 800, and 850 °C. The samples were heated under N_2 at 10 °C/min to reach the desired temperature and kept in isothermal conditions until the reaction was completed (the duration of the isothermal step varies depending on the temperature). During these experiments, the CO_2 release was analyzed by using a mass spectrometer (NETZSCH QMS 403C).

The reversibility of the non-oxidative decarbonation-carbonation was then investigated through decarbonation-carbonation cycles. The temperature was increased from room temperature to 800 °C at a constant heating rate of 10 °C·min^{-1} under N_2 and kept constant for 30 min in N_2 to induce the complete release of the CO_2. The carbonation process was carried out under CO_2 atmosphere with a flow of 50 mL·min^{-1} decreasing the temperature to 400 °C at a constant cooling rate of 10 °C·min^{-1}. Cycling experiments were also performed on the $MnFe_2O_4$–Na_2CO_3 1:1 mixture. To this aim, the temperature was again increased to 800 °C, and the temperature program was repeated depending on the desired number of cycles. A maximum of 10 cycles was performed. The same methodology was subsequently used to test the effect of Mn atomic substitution. The synthesized oxides with 5 and 10 at.% of Ca, Ni, and Zn (see Section 2.1) were mixed with Na_2CO_3 at a 1:1 M ratio. The oxides with 50 at.% of Mn substitution were excluded due to the presence of secondary phases (see structural characterization in the Supporting information).

The substitution of Na_2CO_3 for Li_2CO_3 and K_2CO_3 on reaction 3 was also taken into consideration. The decarbonation/carbonation of equimolar $MnFe_2O_4$–Li_2CO_3 and $MnFe_2O_4$–K_2CO_3 mixtures was investigated by cycling experiments. Heating was performed at 10 °C/min under N_2 (50 mL·min^{-1}); different temperatures were tested with a maximum of 925 °C. After a short isotherm of 10 min, the sample was cooled down to 400 °C at 10 °C/min under 50 mL/min of CO_2. The program was then repeated two more times to get three decarbonation/carbonation cycles.

2.2.2. Hydrogen production

H_2 production experiments were performed using an STA 449 F3 Jupiter (NETZSCH) thermobalance coupled with a water vapor generator provided by aDROP GmbH. The outlet gas of the STA oven was connected to an H_2 Clark-type microsensor (detection limit ≈ 10^{-2} vol%) interfaced with an amplifier (Unisense, Denmark). The sensor was calibrated before each measurement by using a two-point calibration as recommended by the provider. To this aim, pure Ar and an Ar with 2 vol% H_2 standards were used. For each experiment, the desired spinel was mixed with Na_2CO_3 at a 2:3 ratio (see reaction 1) using a mortar and then pressed at 1 ton for 30 s to obtain a 400 mg pellet (d = 10 mm and h ≈ 2 mm). Despite the use of powders would have ensured higher gas-solid interfaces, the use of pellets was necessary to work with a sample size large enough to allow H_2 quantification. The H_2 production experiments were performed as follows. The temperature was increased to 800 °C (10 °C·min^{-1}) and kept constant for 30 min to release 2/3 of the total CO_2 (reaction 3); only Ar flowed during this first part (30 mL/min). Water vapor was then introduced for 90 min at a rate of 1 g H_2O/h while keeping the Ar flow at 30 mL/min. The water supply was then stopped, and the Ar flow was maintained for 10 min to remove the remaining H_2O. CO_2 was then introduced (60 mL/min) and the sample cooled at 10 °C/min. When the temperature reached 400 °C, the gas was then shifted to Ar and the temperature increased again to 800 °C to start a new cycle. A total of 10 cycles were performed. Additional experiments were performed in isothermal conditions at 750 °C and using an H_2 microsensor with a lower detection limit (≈10^{-3} vol%; Unisense, Denmark). The samples were heated at 10 °C/min to 750 °C under a 100 mL N_2 flow. Water vapor was then introduced into the gas flow at a rate of 0.5 g H_2O/h for 5 h. When the water supply was stopped, the N_2 flow was maintained for 5 min to remove the remaining H_2O. CO_2 was then introduced (100 mL/min) and the sample was left at 750 °C overnight. The gas flow was then shifted again to start another WS step. A total of 5 cycles were performed. As the H_2 production was observed to be faster from the second cycle, the 4 remaining WS steps were shortened from 5 to 3 h.

2.3. Structural characterization

The as-synthetized ferrites and the studied mixtures were characterized by X-ray diffraction (XRD) analysis using a Bruker D8 Discover equipped with a LYNXEYE XE detector and a monochromatic Cu Kα1 radiation source of λ = 1.54056 Å. For some mixtures, a sample holder equipped with a Kapton film was used to avoid oxidation and/or hydration during the XRD pattern acquisition. For instance, MnO is very prone to oxidation to Mn^{3+} species and dry K_2CO_3 rapidly forms sesquihydrate K_2CO_3. The use of Kapton results in a strong background at low scattering angles ($10 > 2\theta < 30$). *In situ* XRD measurements were performed at different temperatures using a Bruker D8 Advance diffractometer equipped with a LYNXEYE detector, a Vantec-1 PSD detector, a Co tube (Kα1 of λ = 1.78896; Kβ1 = 1.6210334), and an Anton Parr HTK2000 high-temperature furnace. Patterns were recorded under N_2 atmosphere at room temperature and 400, 450, 500, 550, 600, 700, and 800 °C in a stepwise manner. The decarbonation reaction was analyzed as follows. After a stabilization time of 30 min at 800 °C, CO_2 was then introduced, and the temperature was then maintained at 800 °C for 1 h to guarantee a complete saturation of the chamber. Patterns were then collected at 800, 600 °C, and room temperature in a stepwise manner with a cooling rate of 10 °C/min after each step. Phase identification was performed using the EVA

Table 1
Compositions of the different synthesized oxides together with the abbreviation used in the text.

Composition	Abbreviation
$Mn_{0.95}Ni_{0.05}Fe_2O_4$	5% Ni
$Mn_{0.9}Ni_{0.1}Fe_2O_4$	10% Ni
$Mn_{0.5}Ni_{0.5}Fe_2O_4$	50% Ni
$Mn_{0.95}Zn_{0.05}Fe_2O_4$	5% Zn
$Mn_{0.9}Zn_{0.1}Fe_2O_4$	10% Zn
$Mn_{0.5}Zn_{0.5}Fe_2O_4$	50% Zn
$Mn_{0.95}Ca_{0.05}Fe_2O_4$	5% Ca
$Mn_{0.9}Ca_{0.1}Fe_2O_4$	10% Ca
$Mn_{0.5}Ca_{0.5}Fe_2O_4$	50% Ca

diffraction commercial software. The collected patterns were then analyzed according to the Rietveld method [46] by using the MAUD software [47]. The morphology of the powders before and after carbonation-decarbonation cycles was analyzed using scanning electron microscopy (SEM) using a Quanta 200 FEG (FEI Company, Hillsboro, OR, USA) operating in high vacuum mode.

3. Results and discussion

3.1. Non-oxidative decarbonation reaction of the $MnFe_2O_4$–Na_2CO_3 mixture

The morphology of the as-synthesized oxides was investigated using SEM. Representative images of the $MnFe_2O_4$ are reported in Fig. 1a–b. The obtained powders show a hierarchical network with well-connected macropores due to the consistent amount of gases that is rapidly released during the reaction [48]. The synthesized ferrites were characterized using XRD, and the phase composition and the microstructure were investigated according to the Rietveld method (Section 1 of Supporting information). The obtained powders present a fine microstructure with the average crystallite sizes in the range of 50–100 nm, which is due to the fast cooling experienced during the combustion synthesis. In all cases, the main crystallographic phase is the cubic spinel characteristic of the $MnFe_2O_4$ compound, followed by minor amounts of FeO and MnO (Fig. S1a). Minor amounts of other secondary phases were detected in the samples with 50% of atomic substitution. The atomic substitution also affected the lattice parameter of the cubic spinel phase (Fig. S1a). Different trends were observed depending on the atomic mismatch between the doping element and Mn. While Zn did not induce any significant changes, Ca and Ni led to lattice expansion and shrinkage, respectively.

The non-oxidative decarbonation reaction (3) of the $MnFe_2O_4$–Na_2CO_3 system was investigated under isothermal conditions in the 600–850 °C temperature range. The TPD profiles obtained for the 1:1 mixture at increasing temperatures are reported in Fig. 1c. For all the experiments, a small mass decrease (≈0.5 wt%) is detected at temperatures around 100 °C because of the desorption of absorbed water. The decomposition of the mixture starts at approximately 550 °C and proceeds at different rates depending on the temperature isotherm. As expected from reaction 3, mass spectrometr (MS) analysis of the outlet gases confirms that CO_2 was the only product. The intensity of the characteristic peak of the CO_2^+ ion (44 *m/z*) is reported in Fig. 1d as a function of time. For the sample heated at 600 °C, the decarbonation reaction proceeds very slowly and only a small mass change (≈2 wt%) is detected after more than 300 min. No significant changes can be observed in the MS signal apart from a small peak between 25 and 30 min. As the released CO_2 is diluted in the N_2 carrier gas, it is possible that the resulting concentration was too low to be detected. The reaction proceeds faster at 700 and 750 °C. A significant mass loss is observed, together with an increase of the MS signal that reaches a maximum after 33 and 36 min, respectively. Then, the CO_2 evolution continues at a lower rate and the slope of the mass change profile progressively decreases. After 180 min at 700 °C, a mass loss of about 10 wt% is observed, meaning that the full desorption could not be achieved within a reasonable time at this temperature. On the other hand, a plateau is reached

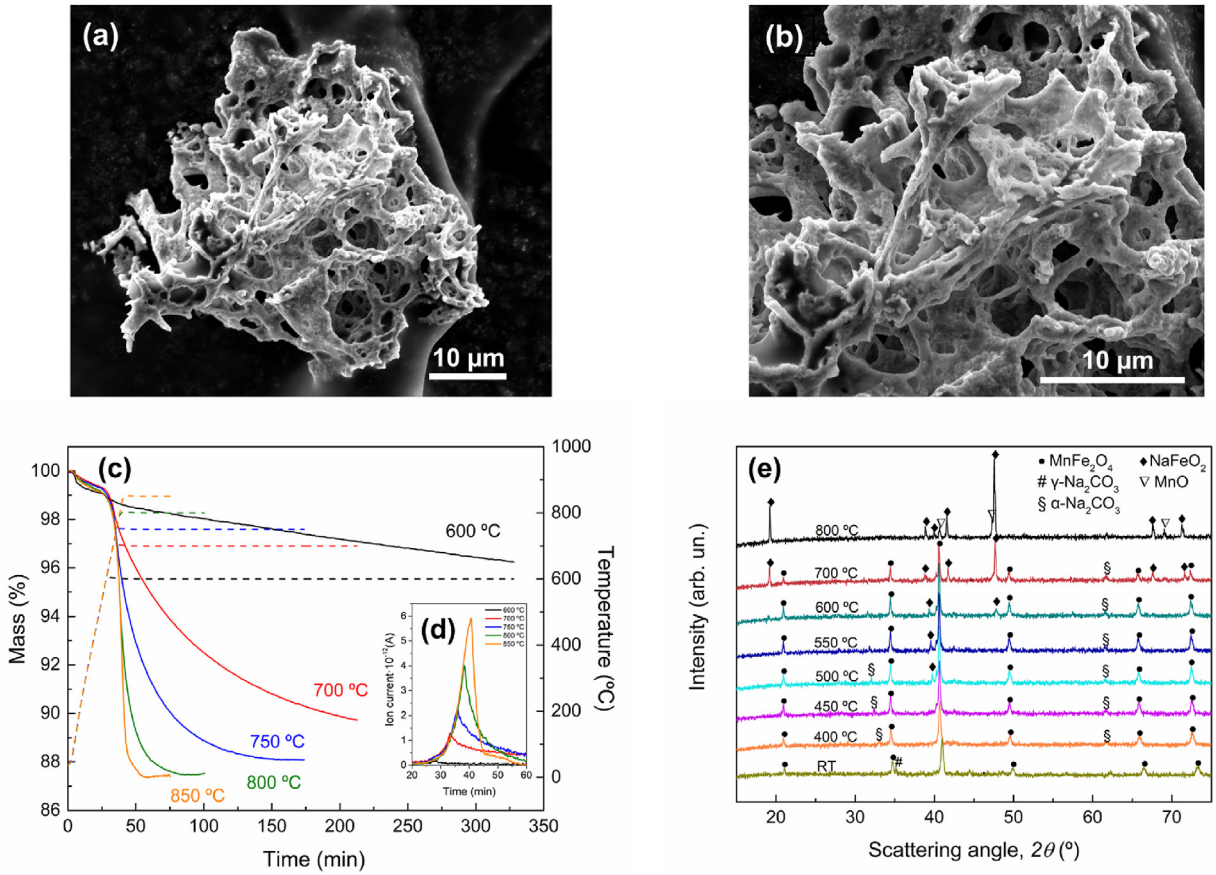

Fig. 1. (a), (b) SEM images of the as-synthesized $MnFe_2O_4$ at different magnifications. **(c)** TPD profiles of the $MnFe_2O_4$–Na_2CO_3 mixture (1:1) in the 600–850 °C temperature range. **(d)** MS signal of the CO_2^+ ion ($m/z = 44$) detected during the isothermal experiments. **(e)** *In situ* XRD patterns of the $MnFe_2O_4$–Na_2CO_3 mixture (1:1) upon heating from RT to 800 °C under N_2. SEM, scanning electron microscopy; TPD, temperature programmed desorption; XRD, X-ray diffraction.

after about 60 min at 750 °C. The overall mass loss is around 12 wt%, which according to reaction 3 is close to the theoretical one (13 wt %). The mixtures heated at 800 and 850 °C follow the previous trend. The maximum CO_2 concentration is revealed after 38 and 40 min, while desorption ends after 85 and 60 min, respectively. In both cases, the mass stabilizes at about 87.5 wt%, thus suggesting that the reaction almost goes to completion.

XRD analysis of the $MnFe_2O_4$–Na_2CO_3 mixture after the TPD at 850 °C is in line with the previous observation (Fig. S2a). About 70 wt% and 25 wt% were obtained for $NaFeO_2$ and MnO, respectively, together with a 5 wt% of unreacted spinel. This agrees with the theoretical values calculated based on reaction 3 (75.5 wt% and 24.5 wt% for $NaFeO_2$ and MnO, respectively) proposed by Varsano et al. [23]. However, the same authors did not observe the formation of MnO due to the highly dispersed and disordered nature of the manganese compound. To obtain further insight, XRD patterns were acquired *in situ* upon heating the $MnFe_2O_4$–Na_2CO_3 under an N_2 atmosphere Fig. 1e. A significant increase in the lattice parameter of the spinel phase can be appreciated due to thermal expansion (Fig. S2b). In addition, the transition of γ-Na_2CO_3 to α-Na_2CO_3 takes place at 400 °C according to what was previously reported [23]. At 600 °C, the $NaFeO_2$ starts forming as highlighted by the peaks at 2θ values of 19 and 47, while MnO is not detected probably due to its low amount. At 700 °C, the amount of $NaFeO_2$ increases while the intensity of the Bragg peaks of $MnFe_2O_4$ significantly reduces. Moreover, a small peak of the MnO can be appreciable at $2\theta = 47$. Finally, the pattern collected at 800 °C confirms that reaction 3 went to completion, as only $NaFeO_2$ and MgO are detected.

The cyclability of the $MnFe_2O_4$–Na_2CO_3 mixture was investigated through 10 consecutive decarbonation/carbonation cycles. An equilibration cycle was initially performed to reduce any difference among the various batches of synthesized spinel. The sample was initially heated up to 800 °C, and this temperature was kept constant for 2 h. Cooling to 400 °C was then carried out under CO_2. This cycle will be referred to as cycle 0. Ten additional cycles were then performed in the 400–800 °C temperature range. The mass profile and the mass changes measured during the decarbonation and carbonation steps are reported in Fig. 2a and b, respectively. During cycle 0, almost full desorption is achieved after about 30 min at 800 °C, with an overall mass loss of around 11.5 wt % (Fig. 2b). A 10 wt% mass increase is observed during the subsequent carbonation step, thus marking a reversibility loss of about 1.5 wt%. A small but constant loss of reversibility is observed from cycle 1 to cycle 4, while the mass change stabilizes at a value around 8 wt% of the initial mass during the following cycles. SEM analysis was carried out after the third desorption step and after three full cycles, i.e., after 455 and 485 min (Fig. 2c–d and Fig. 2e–f, respectively). Partial sintering occurred due to the prolonged exposure to high temperatures, and the sample showed grains ranging from 0.5 to 4 μm with an average value of ≈1.3 μm (Fig. 2c). Despite this, the desorbed sample still presents a significant porosity. A closer look unravels the presence of a laminar structure that can be attributed to the $NaFeO_2$ phase (Fig. 2d) [24]. The sample after the carbonation step shows a more irregular morphology (Fig. 2e–f). The backscattered electron detector highlights the formation of Na_2CO_3 (brighter areas) that results in high contrast with the underlying $MnFe_2O_4$/$NaFeO_2$ matrix. XRD analysis was performed after 10 cycles without showing any parasite phases (Fig. S2f). However, the quantification of the crystallographic phases suggests that after 10 cycles almost half of the initial spinel phase do not participate in the reaction, and rather acts as an inert phase. Based on these results, the loss of reversibility can be explained as follows (see Fig. 2g). As the carbonation reaction takes place and the Na ion are deintercalated from $NaFeO_2$, the regenerated Na_2CO_3 tends to coalesce and covers the newly formed $MnFe_2O_4$. The specific interfaces between $MnFe_2O_4$ and Na_2CO_3 and CO_2 are then reduced, and the subsequent decarbonation reaction is negatively affected. In this sense, phenomena like partial sintering, loss of porosity, and grain growth may further boost this behavior, which explains the loss of reversibility highlighted by thermogravimetry.

3.2. Effect of different alkali carbonates

In this section, we present the effect of the substitution of Na for K and Li on the kinetic and reversibility of the decarbonation-carbonation reaction. A total of three decarbonation-carbonation cycles were sufficient in this case to highlight the difference between the three compositions. The mass profiles of the $MnFe_2O_4$–K_2CO_3 and $MnFe_2O_4$–Li_2CO_3 mixtures (1:1) are compared with the $MnFe_2O_4$–Na_2CO_3 reference system (Fig. 3a–b). The XRD patterns acquired for the three mixtures before and after the three cycles are reported in Fig. 3c. As the behavior of the $MnFe_2O_4$–Na_2CO_3 mixture has been extensively discussed in the previous section, it will not be addressed in the present one and will be only used as the term of comparison to describe the effect of Na substitution for Li and K.

The $MnFe_2O_4$–K_2CO_3 mixture shows a similar onset temperature to the $MnFe_2O_4$–Na_2CO_3 one, but the overall decarbonation kinetic is slower than the reference system (Fig. 3a). During the first desorption step, the mixture with K_2CO_3 shows a 10.8% mass loss, which is slightly lower than the theoretical one (11.9 wt%). As CO_2 is introduced, the carbonation reaction immediately starts and 96.5 wt% of the initial mass is achieved in less than 1 min. A decrease in performance is observed during the following two cycles, and the desorption kinetics of $MnFe_2O_4$–K_2CO_3 further slows down compared to $MnFe_2O_4$–Na_2CO_3. Moreover, the system loses reversibility upon cycling and desorbs 9.38% and 8.73 wt% of its initial mass during the second and third cycle, respectively. The XRD analysis of the $MnFe_2O_4$–K_2CO_3 mixture after three cycles confirms the partial regeneration of the starting reactants, meaning $MnFe_2O_4$ and K_2CO_3 sesquihydrate (COD 2200592). The latter was detected also in the starting mixture and is due to the highly hygroscopic nature of anhydrous K_2CO_3, which causes its rapid hydration during the XRD sample preparation. Moreover, the cycled $MnFe_2O_4$–K_2CO_3 mixture shows a significant amount of potassium beta ferrite, $K_2Fe_{10}O_{16}$ (COD 1529668), which explains the loss of reversibility observed upon cycling. The formation of $KFeO_2$ would be expected if the $MnFe_2O_4$–K_2CO_3 followed reaction 3. However, no $KFeO_2$ could be detected, which suggests a different reaction mechanism compared to the $MnFe_2O_4$–Na_2CO_3 system. It is worth saying that the potassium beta ferrite shows a lamellar structure that allows for a broad range of non-stoichiometric compositions corresponding to different Fe to K ratios [49]. The compensation for non-stoichiometry can be achieved by the inclusion of bivalent atoms, which in this case may be Mn^{2+} [50]. For these reasons, the rationalization of these results to find a reaction mechanism explaining the loss of performances observed in the $MnFe_2O_4$–K_2CO_3 mixture is not straightforward.

The $MnFe_2O_4$–Li_2CO_3 system demonstrates a different behavior. During the first heating step, the system shows impressive performances in terms of kinetics and shows an onset decarbonation temperature of about 100 °C lower than the $MnFe_2O_4$–Na_2CO_3 mixture (Fig. 3a). It starts releasing CO_2 at around 420 °C and almost completes the decarbonation when the $MnFe_2O_4$–Na_2CO_3 and $MnFe_2O_4$–K_2CO_3 mixtures start decarbonizing. The observed overall mass loss is about 11.37 wt%, which is 78% of the 14.4 wt% theoretical value. However, the subsequent exposure to CO_2 does not induce any significant mass increase and the mass of the sample remains almost unvaried during the subsequent two cycles (Fig. 3b). Such poor reversibility of the $MnFe_2O_4$–Li_2CO_3 system is

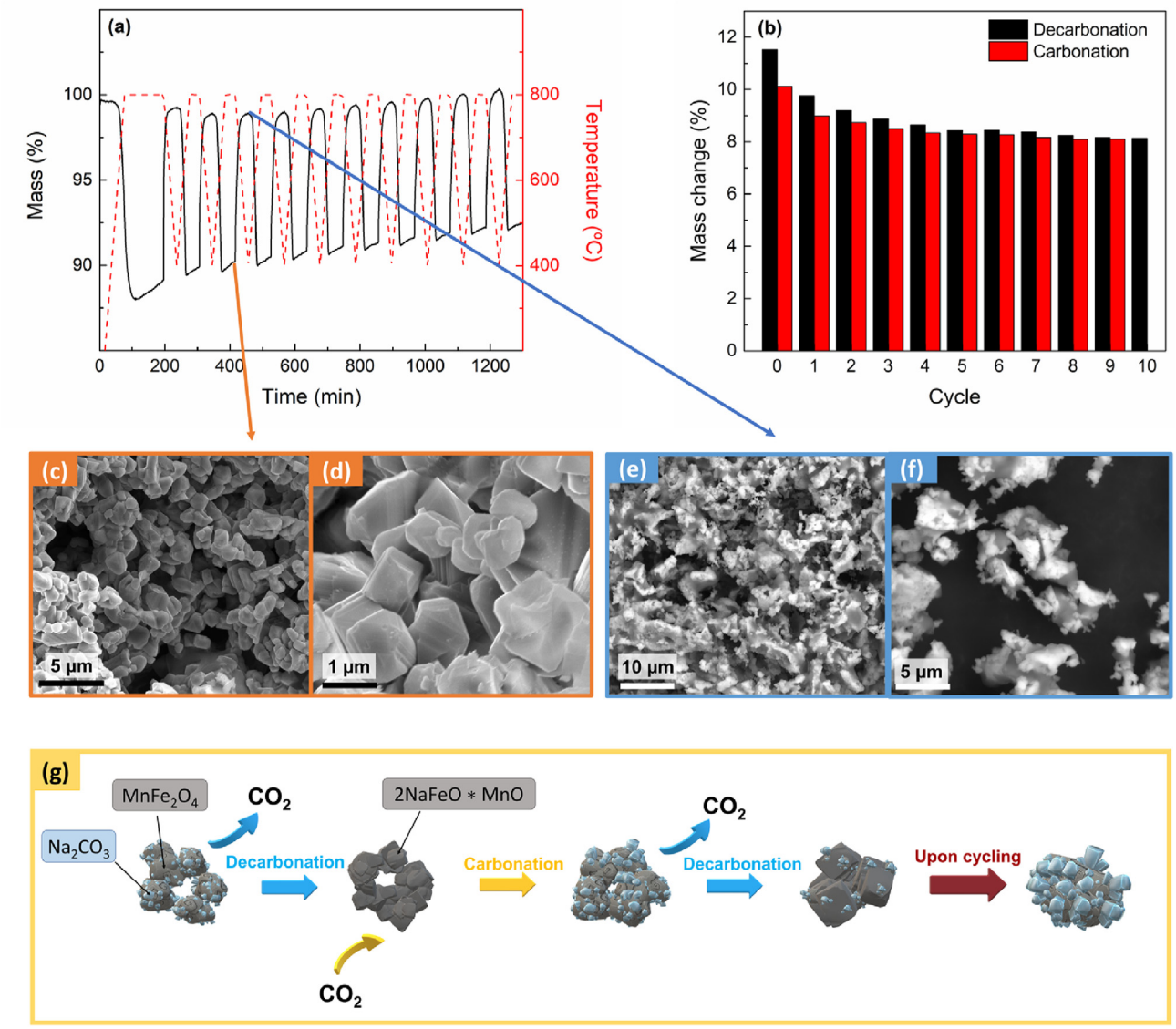

Fig. 2. **(a)** Mass profiles of the $MnFe_2O_4$–Na_2CO_3 mixture during 10 decarbonation-carbonation cycles performed between 800 °C and 400 °C. **(b)** Mass change related to decarbonation and carbonation steps during the cycles. **(c–f)** SEM images of the $MnFe_2O_4$–Na_2CO_3 mixture after cycle 3. The images were acquired after the third decarbonation **(c–d)** and **(e–f)** after the third carbonation steps, respectively. **(g)** Schematic representation of the sintering and phase coalescence processes that lead to the decrease of reversibility during the first cycles. SEM, scanning electron microscopy.

confirmed by the XRD analysis (Fig. 3c), which highlights the presence of $MnFe_2O_4$ and cubic $LiFeO_2$ (COD 1541312). Thus, it seems that the reaction follows the mechanism of reaction 3, with $LiFeO_2$ being formed instead of $NaFeO_2$. However, the subsequent deintercalation of Li ions seems to be hindered probably due to the strong Li–O bond. As result, reaction 3 is irreversible at the present experimental conditions for the $MnFe_2O_4$–Li_2CO_3 system. The XRD quantitative analysis indicates 49 wt% and 51 wt% for $MnFe_2O_4$ and $LiFeO_2$, respectively. Considering the molar mass of the two compounds, this means that the molar ratio between $MnFe_2O_4$ and $LiFeO_2$ is around 1:2.5. If the stoichiometry of reaction 3 is valid also for the $MnFe_2O_4$–Li_2CO_3 system, this means that only about 55% of the initial mixture reacted. This would imply a mass loss of only 7.9 wt%, which is lower than the experimentally observed and suggests that some cross-reaction may have taken place. Moreover, the spinel phase in the $MnFe_2O_4$–Li_2CO_3 cycled mixture has an average lattice parameter of 8.38 Å, which is significantly lower than the one observed for the $MnFe_2O_4$–Na_2CO_3 cycled in the same experimental conditions (8.53 Å). This has at least two possible explanations. First, Fe_3O_4 is formed rather than $MnFe_2O_4$; indeed, the two compounds share the same crystal structure with the only difference being the larger lattice parameter of $MnFe_2O_4$ as a consequence of Fe^{2+} substitutions for the bigger Mn^{2+}. However, the formation of Fe_3O_4 would imply the reduction of part of Fe^{3+} to Fe^{2+} at the expenses of Mn^{2+} that should be oxidized to form $NaMnO_2$ or other secondary compounds, which were not detected. Another possibility is that the $MnFe_2O_4$ lattice has shrunk due to a partial Li^+ substitution or intercalation, as the atomic substitution for low electronegative cations was reported to induce a decrease in spinel lattice parameters [51–53].

Resuming, the $MnFe_2O_4$–Na_2CO_3 mixture showed better performances than both $MnFe_2O_4$–Li_2CO_3 and $MnFe_2O_4$–K_2CO_3. Indeed, the former showed almost negligible reversibility caused by the irreversible formation of $LiFeO_2$, while the latter showed worse kinetics and reversibility due to the formation of potassium beta ferrite. For these reasons, the $MnFe_2O_4$–Na_2CO_3 was kept as

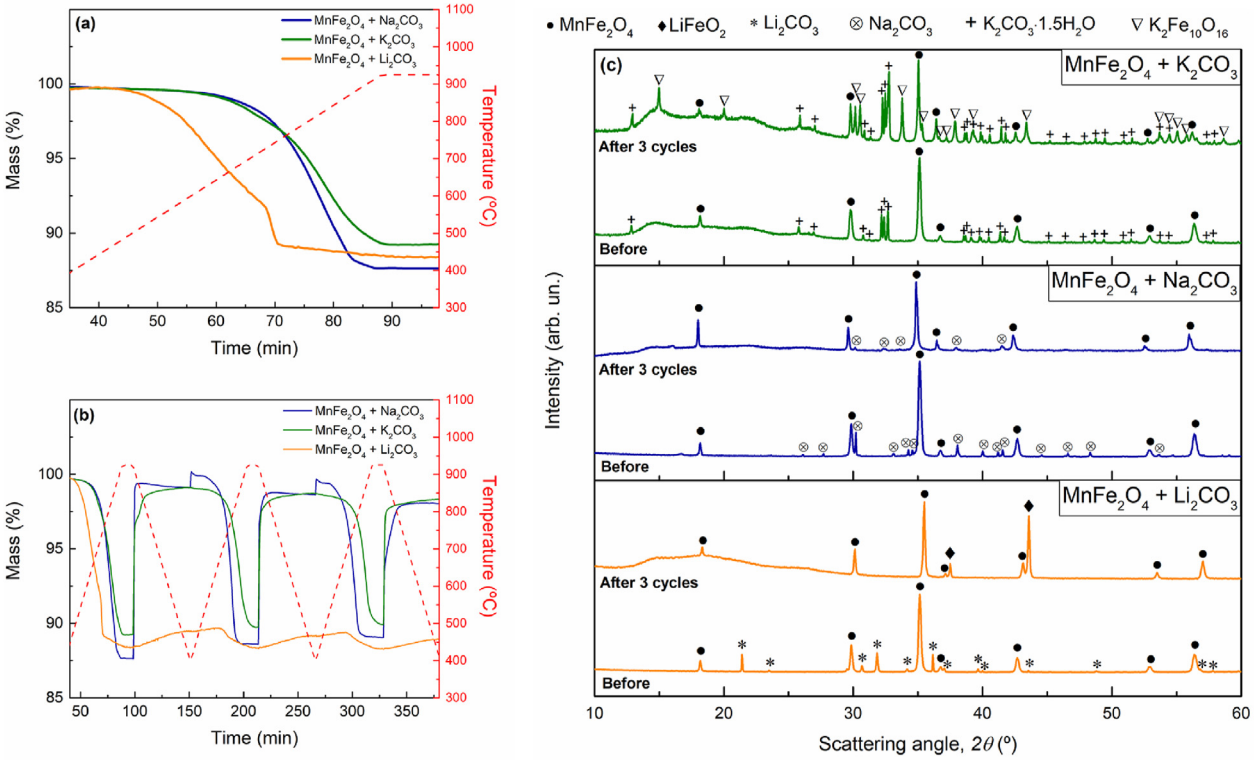

Fig. 3. Mass profiles of the $MnFe_2O_4$–Na_2CO_3, $MnFe_2O_4$–Li_2CO_3, and $MnFe_2O_4$–K_2CO_3 mixtures during **(a)** the first decarbonation step and **(b)** during 3 decarbonation-carbonation cycles. **(c)** XRD patterns collected for the three mixtures before and after 3 cycles. XRD, X-ray diffraction.

the starting reference system to investigate the atomic-substituted spinel ferrites that are presented in the following section.

3.3. Effect of Mn substitution

In this section, the effect of partial substitution of Mn for Zn, Ni, and Ca on the decarbonation-carbonation reaction is presented. Samples at 5 and 10 at.% of Zn Ni, and Ca were cycled 10 times. Data are reported in Fig. 4 by taking the $MnFe_2O_4$–Na_2CO_3 mixtures as the reference system. In the first cycle, the three 5 at.%-doped samples show slightly better decarbonation kinetics than the undoped system, which can be appreciated by the small left shift of the mass profiles in the time scale (Fig. S3a). However, such difference is no further appreciated in the fifth and ninth cycles (Fig. S3b and c), as the four decarbonation profiles almost overlap. Same thing for the carbonation kinetics; the small differences between the four samples that are observed during the first cycle, progressively vanish as the number of cycles increases.

Major differences can be appreciated concerning the amount of desorbed CO_2, as can be appreciated in Fig. 4a. In the first cycle, the undoped $MnFe_2O_4$ shows the highest mass loss (9.76 wt%), followed by the 5% Ni, 5% Zn, and 5% Ca ferrites, which exhibit a mass loss of 8.8, 8.15, and 6.8 wt%, respectively. However, the undoped $MnFe_2O_4$ progressively loses capacity while the three doped ferrites seem to suffer less reversibility loss, with the Zn-doped sample even showing a slight increase in performance. After 10 cycles, the undoped $MnFe_2O_4$ and the 5% Ni samples show a similar behavior, as they lose 8.14 wt% and 8.2 wt%, respectively. The Ca-doped sample desorbs only 6.5 wt%, while the Zn-doped leads to the highest mass loss (8.6 wt%).

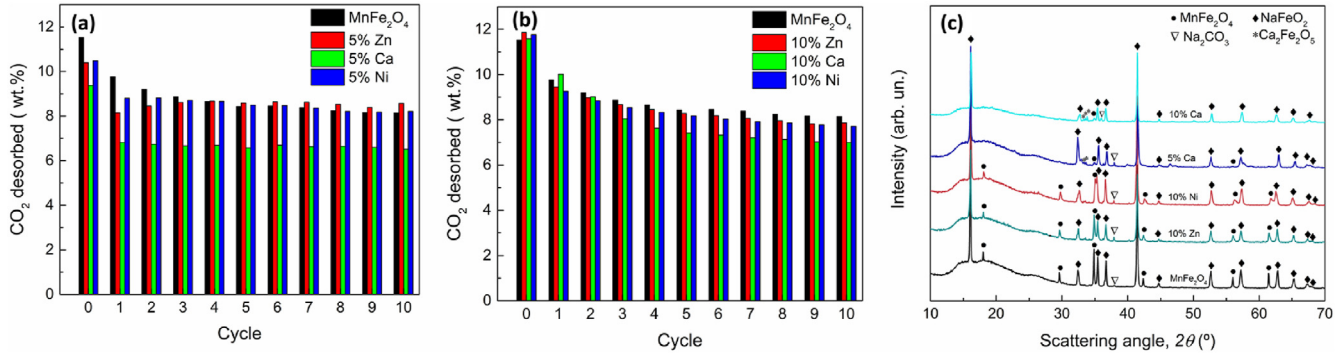

Fig. 4. The effect of 5 and 10 at.% Ca, Ni, and Zn atomic substitution on the $MnFe_2O_4$–Na_2CO_3 mixture during 10 decarbonation-carbonation cycles. **(a)** The measured CO_2 release during 10 cycles for the 5 at.% Ca, Ni, and Zn-doped ferrites, and **(b)** for the 10 at.% Ca, Ni, and Zn-doped ferrites. **(c)** XRD patterns of different $Mn_{1-x}A_xFe_2O_4$–Na_2CO_3 mixtures after 10 decarbonation-carbonation cycles. XRD, X-ray diffraction.

Data of the mixtures with 10 at.% of Zn, Ni, and Ca are reported in Fig. 4b and Fig. S3d. Overall, the increase in atomic substitution from 5% to 10% does not lead to any significant change. After 9 cycles, the three substituted ferrites exhibit a slight worsening in the mass loss rate in comparison to pure $MnFe_2O_4$ (Fig. S3d), while the carbonation reaction proceeds faster. Among the doped ferrites, no significant differences can be appreciated in terms of kinetic performances. On the other hand, the dopant element affects the reversibility as the 10% Zn and 10% Ni ferrites show a similar weight loss during all the cycles, while the substitution for Ca results in a lower CO_2 release. All the samples show a loss of reversibility that is more evident during the first cycles. After 10 cycles, pure $MnFe_2O_4$ shows the highest desorption, followed by 10% Zn, 10% Ni, and 10% Ca samples that lose 7.9 wt%, 7.8 wt%, and 7 wt%, respectively.

According to the XRD analysis, the partial Mn substitution for Ni and Zn did not induce significant changes in the phase composition of the mixtures (Fig. 4c). No appreciable amounts of secondary phases were detected suggesting that the initial fine dispersion of the dopants was retained even upon prolonged cycling. On the other hand, the XRD patterns of both the 5 at.% and 10 at.% Ca-doped ferrites show the formation of $Ca_2Fe_2O_5$ as a parasite phase, which explains the decrease in performances observed during the cycles.

The XRD patterns of the different $Mn_{1-x}A_xFe_2O_4$—Na_2CO_3 mixtures were refined to get further insight. The average lattice parameter of the two main phases, i.e. the cubic $MnFe_2O_4$ and the trigonal $NaFeO_2$, are reported in Fig. S3e and f, respectively. Overall, a general decrease of the two lattice parameters is observed as the amount of dopant increases. While this behavior is less evident for Zn ferrites, it becomes way more significant for the samples doped with Ni and Ca. Data obtained for Zn and Ni samples are in line with what was expected, as a similar trend was observed for the lattice parameter of the as-synthesized Ni and Zn ferrites (Section S1 Fig. S1b). On the contrary, data are more difficult to interpret in the case of Ca-doped ferrites. Indeed, the as-synthesized Ca—$MnFe_2O_4$ samples showed a significant lattice expansion due to the larger Ca^{2+} ions in comparison to Mn^{2+}. For this reason, the lattice shrinkage detected after 10 cycles would not be expected. A possible interpretation can be found in the precipitation of the $Ca_2Fe_2O_5$ phase, which may lead to the formation of a high concentration of vacancies in the $NaFeO_2$ phase. In general, a straightforward connection between the lattice volume and the decarbonation-carbonation performances can be excluded for the three systems investigated.

3.4. Hydrogen production

Among the composition investigated in the previous section, the spinel with 5% of Zn showed the best reversibility during the decarbonation-carbonation cycles. This composition was then selected for WS experiments. In the following, the H_2 production of the $Zn_{0.05}Mn_{0.95}Fe_2O_4$—$Na_2CO_3$ system is presented, while using the $MnFe_2O_4$—Na_2CO_3 mixture as a reference (Fig. 5).

The samples were initially tested in dynamic conditions, by modifying the temperature program used in the decarbonation-carbonation cycles (see Section 2.2). The two mixtures were cycled ten times to investigate the reversibility of the H_2 production reaction. The first WS step is reported in detail in Fig. 5a, where the mass profiles are shown together with the H_2 evolution. The gas flow composition corresponding to each step of the experiment is also reported to facilitate data interpretation. During the first 100 min of the experiment, no water vapor was introduced. As previously carried out for the 1:1 mixtures, the samples were heated to 800 °C and kept under isothermal conditions for 30 min.

As can be appreciated in Fig. 5a, an initial small mass loss of 0.45 and 0.75 wt% is observed for undoped and Zn-doped mixtures, respectively; this is likely due to the desorption of some residual moisture from Na_2CO_3 powders, which are highly hygroscopic. As expected, both mixtures start releasing CO_2 at around 550 °C; the mass loss rate first increases and then approaches a plateau after around 30 min at 800 °C. In this regard, the sample with 5% of Zn shows a better kinetic than the undoped $MnFe_2O_4$, as well as a higher CO_2 desorption (12. wt.% vs 10 wt%). Such values are in line with the theoretical mass loss expected for the release of 2/3 of the total CO_2, which according to reaction 1, corresponds to a weight loss of 11.3 wt%. This confirms the mechanism proposed by Varsano et al. and resumed in the introduction (reactions 3 and 4) [23]. As soon as water vapor is introduced, the masses of the two samples start to decrease again and H_2 is suddenly detected. The amount of H_2 increases and reaches a maximum of 22.3 and 12.6 μmol g^{-1} s^{-1} for pure and 5% Zn $MnFe_2O_4$, respectively. Even if at a lower rate, H_2 production continues for both samples as long as water vapor is supplied. In the meantime, the masses of the two samples keep decreasing and stabilize at around 85% of the initial value. An overall mass loss of 14.4 wt% and 15.2 wt% is detected for the undoped and Zn-doped mixtures, respectively. According to the stoichiometry of reaction 1, theoretical mass losses of 14.9 and 15 wt% are expected for the undoped and Zn-doped mixtures, respectively. These values are given by the sum of two different contributions. First, the CO_2 release due to the decomposition of Na_2CO_3, which corresponds to a 16.9 wt% mass loss. Second, the O_2 uptake from the reaction with water steam to form the $NaMn_{1/3}Fe_{2/3}O_2$, which corresponds to a 2 wt% mass gain. The second contribution is linked to the oxidation of Mn^{2+} to Mn^{3+} and, in turn, to the H_2 production. As Zn does not contribute to the redox process, a 5%-lower mass change is expected for the 5% Zn spinel—i.e. +1.9 wt%. Considering the additional mass change that is due to the initial moisture desorption, a maximum mass loss of 15.35 and 15.78 wt% are reasonably expected for the undoped and the Zn-doped mixtures; comparing the experimental data with these values, conversions of 93.8% and 96.3%, respectively, were obtained.

The data obtained from the thermobalance were compared with those obtained from the H_2 microsensor. In particular, the integration of the H_2 production over time provided H_2 yields of 1.14 mmol/g for pure $MnFe_2O_4$ and 0.66 mmol/g for 5% Zn $MnFe_2O_4$. As the theoretical yield for the $MnFe_2O_4$—Na_2CO_3 mixture is 1.28 mmol/g, a relative H_2 yield of ≈89% is obtained, which agrees with the value obtained from thermogravimetric data. On the other hand, the Zn-doped mixture marks an H_2 yield of 54% only, with its theoretical H_2 yield being 1.21 mmol/g. Such value is significantly lower than the one calculated based on thermogravimetry and it is counterintuitive at a first glance. In fact, as the Zn-doped spinel showed a higher mass loss than the undoped, one would expect a higher H_2 yield for the former. Such results can be interpreted by recalling the different contributions to the mass change, meaning CO_2 release and O_2 uptake.

The overall difference between the experimentally observed mass loss of the Zn-doped and that of the undoped mixture is 0.8 wt%. This value reduces to 0.5 wt% when considering the contributions of the initial moisture desorption. XRD analysis was performed after the first WS step (Fig. S4a). For both mixtures, $NaMn_{1/3}Fe_{2/3}O_2$ was identified as the main phase, followed by minor amounts of unreacted Na_2CO_3 and $MnFe_2O_4$. It is then reasonable to assume that the CO_2 release of the 5% Zn-doped mixture took place with no significant changes compared to the undoped. The difference in terms of mass loss between the two mixtures is then related only to the O_2 uptake, which is also supported by the high difference in terms of produced H_2. After a few

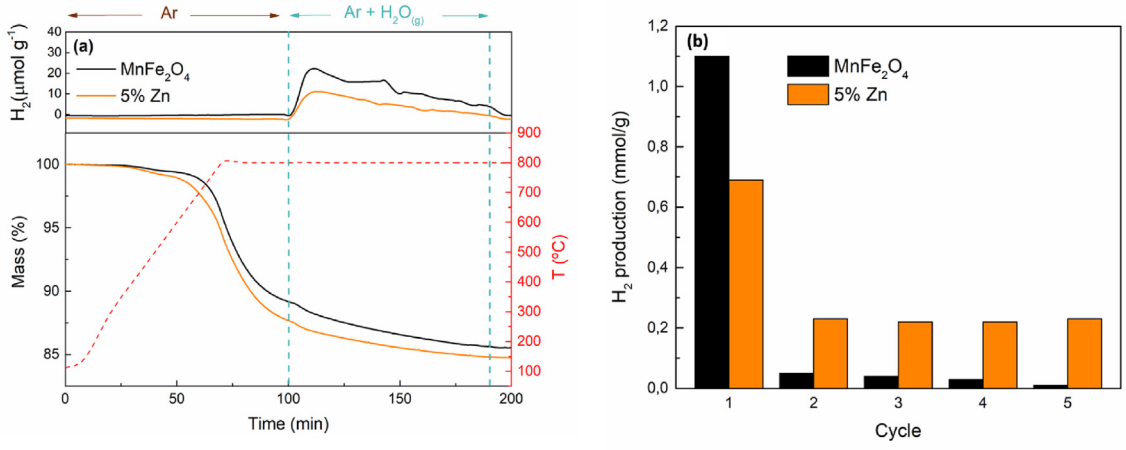

Fig. 5. **(a)** Mass profiles and H_2 evolution of the $MnFe_2O_4$–Na_2CO_3 and 5% Zn $MnFe_2O_4$–Na_2CO_3 mixtures during the first WS step at 800 °C. **(b)** H_2 production (mmol H_2/g) of the undoped $MnFe_2O_4$–Na_2CO_3 and the 5% Zn-doped mixtures during 5 cycles at 750 °C.

simple proportions, this leads to a relative H_2 yield of 63%, which is in better agreement with the value obtained by the direct integration of the H_2 signal.

During the subsequent cycling in dynamic conditions, the Zn-doped mixture showed a better reversibility in terms of mass change (Fig. S4b) that also corresponded to a significantly lower amount of undesired secondary phases such as the non-stoichiometric $Na_xMn_3O_7$ (Fig. S4c). However, H_2 was not detected during the following 9 cycles for both samples. Despite this, the presence of significant amounts of $MnFe_2O_4$ and Na_2CO_3 in the cycled mixtures suggests that even if with a lower yield, H_2 was produced also during the remaining cycles. A possible explanation is that the incomplete regeneration of the reactants lowered the H_2 production so that the H_2 concentration was lower than the detection limit of the microsensor used. A more detailed discussion is provided in Section 4.1 of the supporting Information file.

Despite the effect of Zn-doping on the H_2 production could not be directly evaluated in the above-mentioned experimental conditions, both XRD and thermogravimetry suggested a positive effect of Zn on the reversibility. To shed light on this, both the undoped $MnFe_2O_4$–Na_2CO_3 and the 5% Zn-doped $MnFe_2O_4$–Na_2CO_3 mixtures were subsequently tested in isothermal conditions at 750 °C for a total of 5 cycles (Section 2.2.2 for details). The H_2 production of the two mixtures is reported in Table 2, and the data are plotted in Fig. 5b. As seen before for the experiments at 800 °C, the undoped $MnFe_2O_4$–Na_2CO_3 mixture produces more H_2 during the first cycle (86% yield). However, its H_2 production drastically decreases by two orders of magnitude in the second cycle and keeps decreasing during the following three. Eventually, almost no H_2 is detected in the fifth cycle. On the other hand, the Zn-doped mixture produces less H_2 during the first cycle (54% yield) but its production stays one order of magnitude higher than the undoped mixture during the following 4 cycles. Moreover, exempt from a first drop after the first cycle, no decreasing tendency can be observed in the following cycles, and the Zn-doped mixture shows a stable H_2 production of ≈0.2 mmol/g from cycle 2 to cycle 5. High reversibility is observed also in terms of kinetic, as the H_2 production profiles from cycles 2 to 5 almost perfectly overlap (Fig. S5). This is also in line with the high reversibility observed in terms of desorbed/captured CO_2 (Table S1). As a result of the two very different behaviors, the difference in terms of H_2 production performances between the two mixtures becomes more evident during the cycles. In the second cycle, the Zn-doped mixture produces 4.6 times more H_2 than the undoped one, while in the fifth cycle, it produces 23 times more. This completely different trend also affects the cumulative H_2 production, which is higher for the Zn-doped mixture (1.60 vs. 1.24 mmol/g).

Table 2
H_2 production (mmol H_2/g) of the undoped $MnFe_2O_4$–Na_2CO_3 and the 5% Zn-doped mixtures during 5 cycles at 750 °C.

Mixture	Hydrogen production (mmol H_2/g)					
	Cycle 1	Cycle 2	Cycle 3	Cycle 4	Cycle 5	Total
$MnFe_2O_4$	1.10	0.05	0.04	0.03	0.01	1.24
5% Zn	0.69	0.23	0.22	0.22	0.23	1.60

4. Conclusions

In the present work, we studied the effect of atomic substitution on the sodium manganese ferrite thermochemical cycle for H_2 production. The decarbonation/carbonation of the $MnFe_2O_4$–Na_2CO_3 mixture was investigated as a starting reference, while both Na and Mn substitution were subsequently considered. Na substitution for K led to a decrease in performance that was attributed to the formation of potassium beta ferrite as an undesired phase. On the other hand, the use of Li decreased the onset decarbonation temperature by about 100 °C, but negligible reversibility was observed under the explored experimental conditions. Despite this, the substitution of Na for Li is promising for decreasing the operating temperature of the thermochemical cycle and deserves further investigation.

Mn partial substitution for Ca, Ni, and Zn improved the rate of the carbonation reaction. The $Mn_{0.95}Zn_{0.05}Fe_2O_4$–$Na_2CO_3$ mixture showed the best reversibility and was tested for H_2 production, while the undoped mixture was used as the reference. During the first cycle, maximum instantaneous H_2 production rates of 22.3 and 12.6 μmol g^{-1} s^{-1} were observed for the undoped and the Zn-doped samples. After 1.5 h at 800 °C, the $MnFe_2O_4$–Na_2CO_3 mixture reached 89% of the theoretical yield, with an overall H_2 production of 1.14 mmol/g. On the other hand, only 0.66 mmol H_2/g (54% conversion) were produced during the same time by the Zn-doped mixture. In both cases, cycling in dynamic conditions (800–400 °C) did not ensure a complete regeneration of the

starting materials and the H_2 produced during the following cycles was under the detection limit. Despite this, both thermogravimetry and XRD analysis highlighted that doping with Zn improved the reversibility upon cycling. This was further confirmed by H_2 production experiments that were performed in isothermal conditions at 750 °C. Despite the $MnFe_2O_4$–Na_2CO_3 mixture produced more H_2 during the first cycle, its production monotonically dropped upon cycling and became almost negligible after only 5 cycles. On the other hand, the Zn-doped mixture shows remarkably stable H_2 production of 0.2 mmol/g with no decreasing trend observed from cycles 2 to 5. As result, its H_2 production after 5 cycles is around 23 times higher than the reference system.

Credit authorship contribution statement

Francesco Torre: data curation, investigation, formal analysis, methodology, writing - original draft & review & editing. **Teresa Aguilar Sanchez:** data curation, investigation, formal analysis, methodology. **Stefania Doppiu:** conceptualization, data curation, funding acquisition, supervision, project administration, writing - review & editing. **Mikel Oregui Bengoechea:** investigation, writing - review & editing. **Pedro Luis Arias Ergueta:** supervision, writing - review & editing. **Elena Palomo del Barrio:** conceptualization, funding acquisition, supervision, writing - review & editing.

Data availability

The raw/processed data required to reproduce these findings cannot be shared at this time as the data also forms part of an ongoing study.

Declaration of competing interest

The authors declare that they have no known competing financial interests or personal relationships that could have appeared to influence the work reported in this paper.

Acknowledgment

This Project is funded by the Department of Economic Development, Sustainability and Environment of the Basque Government (CICe 2019 - KK-2019/00097- and H2BASQUE - KK-2021/00054). The authors express their sincere gratitude to Cristina Luengo and Mikel Intxaurtieta for their technical support.

Appendix A. Supplementary data

Supplementary data to this article can be found online at https://doi.org/10.1016/j.mtener.2022.101094.

References

[1] R.S. El-Emam, H. Özcan, Comprehensive review on the techno-economics of sustainable large-scale clean hydrogen production, J. Clean. Prod. 220 (2019) 593–609, https://doi.org/10.1016/j.jclepro.2019.01.309.
[2] J.E. Lee, I. Shafiq, M. Hussain, S.S. Lam, G.H. Rhee, Y.K. Park, A review on integrated thermochemical hydrogen production from water, Int. J. Hydrogen Energy 47 (2022) 4346–4356, https://doi.org/10.1016/j.ijhydene.2021.11.065.
[3] A. Boretti, J. Nayfeh, A. Al-Maaitah, Hydrogen production by solar thermochemical water-splitting cycle via a beam down concentrator, Front. Energy Res. 9 (2021), 666191, https://doi.org/10.3389/fenrg.2021.666191.
[4] A. Kogan, Direct solar thermal splitting of water and on-site separation of the products - II. Experimental feasibility study, Int. J. Hydrogen Energy 23 (1998) 89–98, https://doi.org/10.1016/s0360-3199(97)00038-4.
[5] F. Safari, I. Dincer, A review and comparative evaluation of thermochemical water splitting cycles for hydrogen production, Energy Convers. Manag. 205 (2020), 112182, https://doi.org/10.1016/j.enconman.2019.112182.
[6] S. Abanades, Metal oxides applied to thermochemical water-splitting for hydrogen production using concentrated solar energy, ChemEngineering 3 (2019) 63, https://doi.org/10.3390/chemengineering3030063.
[7] Y. Mao, Y. Gao, W. Dong, H. Wu, Z. Song, X. Zhao, J. Sun, W. Wang, Hydrogen production via a two-step water splitting thermochemical cycle based on metal oxide – a review, Appl. Energy 267 (2020), 114860, https://doi.org/10.1016/j.apenergy.2020.114860.
[8] C. Herradón, R. Molina, J. Marugán, J.Á. Botas, Experimental assessment of the cyclability of the Mn2O3/MnO thermochemical cycle for solar hydrogen production, Int. J. Hydrogen Energy 44 (2019) 91–100, https://doi.org/10.1016/j.ijhydene.2018.06.158.
[9] R.R. Bhosale, G. Takalkar, P. Sutar, A. Kumar, F. AlMomani, M. Khraisheh, A decade of ceria based solar thermochemical H2O/CO2 splitting cycle, Int. J. Hydrogen Energy 44 (2019) 34–60, https://doi.org/10.1016/j.ijhydene.2018.04.080.
[10] P. Charvin, S. Abanades, F. Lemont, G. Flamant, Experimental study of SnO2/SnO/Sn thermochemical systems for solar production of hydrogen, AIChE J. 54 (2008) 2759–2767, https://doi.org/10.1002/aic.11584.
[11] A. Steinfeld, Solar hydrogen production via a two-step water-splitting thermochemical cycle based on Zn/ZnO redox reactions, Int. J. Hydrogen Energy 27 (2002) 611–619, https://doi.org/10.1016/S0360-3199(01)00177-X.
[12] A. Steinfeld, S. Sanders, R. Palumbo, Design aspects of solar thermochemical engineering - a case study: two-step water-splitting cycle using the Fe3O4/FeO redox sysTEM, Sol. Energy 65 (1999) 43–53, https://doi.org/10.1016/S0038-092X(98)00092-9.
[13] M. Romero, A. Steinfeld, Concentrating solar thermal power and thermochemical fuels, Energy Environ. Sci. 5 (2012) 9234–9245, https://doi.org/10.1039/c2ee21275g.
[14] Y. Deng, R. Dewil, L. Appels, S. Li, J. Baeyens, J. Degrève, G. Wang, Thermochemical water splitting: selection of priority reversible redox reactions by multi-attribute decision making, Renew. Energy 170 (2021) 800–810, https://doi.org/10.1016/j.renene.2021.02.009.
[15] Y. Tamaura, Y. Ueda, J. Matsunami, N. Hasegawa, M. Nezuka, T. Sano, M. Tsuji, Solar hydrogen production by using ferrites, Sol. Energy 65 (1999) 55–57, https://doi.org/10.1016/S0038-092X(98)00087-5.
[16] H. Kaneko, Y. Ochiai, K. Shimizu, Y. Hosokawa, N. Gokon, Y. Tamaura, Thermodynamic study based on the phase diagram of the Na2O-MnO-Fe2O3 system for H2 production in three-step water splitting with Na2CO3/MnFe2O4/Fe2O3, Sol. Energy 72 (2002) 377–383, https://doi.org/10.1016/S0038-092X(02)00012-9.
[17] C. Alvani, A. La Barbera, G. Ennas, F. Padella, F. Varsano, Hydrogen production by using manganese ferrite: evidences and benefits of a multi-step reaction mechanism, Int. J. Hydrogen Energy 31 (2006) 2217–2222, https://doi.org/10.1016/j.ijhydene.2006.02.025.
[18] L. Seralessandri, F. Varsano, A. La Barbera, F. Padella, On the oxygen-releasing step in the water-splitting thermochemical cycle by MnFe2O4-Na2CO3 system, Scripta Mater. 55 (2006) 875–877, https://doi.org/10.1016/j.scriptamat.2006.07.057.
[19] L. Seralessandri, M. Bellusci, C. Alvani, A. La Barbera, F. Padella, F. Varsano, Chemical equilibria involved in the oxygen-releasing step of manganese ferrite water-splitting thermochemical cycle, J. Solid State Chem. 181 (2008) 1992–1997, https://doi.org/10.1016/j.jssc.2008.04.014.
[20] C. Alvani, M. Bellusci, A. La Barbera, F. Padella, M. Pentimalli, L. Seralessandri, F. Varsano, Reactive pellets for improved solar hydrogen production based on sodium manganese ferrite thermochemical cycle, J. Sol. Energy Eng. Trans. ASME 131 (2009), 031015, https://doi.org/10.1115/1.3142723.
[21] C. Alvani, M. Bellusci, A. La Barbera, F. Padella, L. Seralessandri, F. Varsano, Progress in understanding factors governing the sodium manganese ferrite thermochemical cycle, J. Sol. Energy Eng. Trans. ASME 132 (2010), 031001, https://doi.org/10.1115/1.4001401.
[22] F. Varsano, F. Padella, A. La Barbera, C. Alvani, The carbonatation reaction of layered Na(Mn1/3Fe 2/3)O2: a high temperature study, Solid State Ionics 187 (2011) 19–26, https://doi.org/10.1016/j.ssi.2011.02.009.
[23] F. Varsano, F. Padella, C. Alvani, M. Bellusci, A. La Barbera, Chemical aspects of the water-splitting thermochemical cycle based on sodium manganese ferrite, Int. J. Hydrogen Energy 37 (2012) 11595–11601, https://doi.org/10.1016/j.ijhydene.2012.05.042.
[24] M.A. Murmura, F. Varsano, F. Padella, A. La Barbera, C. Alvani, M.C. Annesini, Hydrogen production by the sodium manganese ferrite thermochemical cycle-experimental rate and modeling, Ind. Eng. Chem. Res. 53 (2014) 10310–10317, https://doi.org/10.1021/ie500940z.
[25] F. Varsano, M.A. Murmura, B. Brunetti, F. Padella, A. La Barbera, C. Alvani, M.C. Annesini, Hydrogen production by water splitting on manganese ferrite-sodium carbonate mixture: feasibility tests in a packed bed solar reactor-receiver, Int. J. Hydrogen Energy 39 (2014) 20920–20929, https://doi.org/10.1016/j.ijhydene.2014.10.105.
[26] A. Haeussler, A. Julbe, S. Abanades, Investigation of reactive perovskite materials for solar fuel production via two-step redox cycles: thermochemical activity, thermodynamic properties and reduction kinetics, Mater. Chem. Phys. 276 (2022), 125358, https://doi.org/10.1016/j.matchemphys.2021.125358.
[27] P. Reñones, M.C. Alvarez-Galvan, L. Ruiz-Matas, M. Retuerto, R.M. Navarro, J.L.G. Fierro, Nickel ferrite supported on calcium-stabilized zirconia for solar hydrogen production by two-step thermochemical water splitting, Mater.

Today Energy 6 (2017) 248–254, https://doi.org/10.1016/j.mtener.2017.10.007.
[28] J. Gao, Y. Zhang, X. Wang, L. Jia, H. Jiang, M. Huang, A. Toghan, Nitrogen-doped Sr2Fe1.5Mo0.5O6-δ perovskite as an efficient and stable catalyst for hydrogen evolution reaction, Mater. Today Energy 20 (2021), 100695, https://doi.org/10.1016/j.mtener.2021.100695.
[29] M. Moniruddin, B. Ilyassov, X. Zhao, E. Smith, T. Serikov, N. Ibrayev, R. Asmatulu, N. Nuraje, Recent progress on perovskite materials in photovoltaic and water splitting applications, Mater. Today Energy 7 (2018) 246–259, https://doi.org/10.1016/j.mtener.2017.10.005.
[30] M.B. Kanoun, S. Goumri-Said, Insights into the impact of Mn-doped inorganic CsPbBr3 perovskite on electronic structures and magnetism for photovoltaic application, Mater. Today Energy 21 (2021), 100796, https://doi.org/10.1016/j.mtener.2021.100796.
[31] J. Ge, D. Zhang, J. Jin, X. Han, Y. Wang, F. Zhang, X. Lei, Oxygen atoms substituting sulfur atoms of MoS2 to activate the basal plane and induce the phase transition for boosting hydrogen evolution, Mater. Today Energy 22 (2021), 100854, https://doi.org/10.1016/j.mtener.2021.100854.
[32] E. Soto, F. Vaquero, N. Mota, S. Fateixa, T. Trindade, R.M. Navarro, J.L.G. Fierro, Structure and photoactivity for hydrogen production of CdS nanorods modified with In, Ga, Ag-In and Ag-Ga and prepared by solvothermal method, Mater. Today Energy 9 (2018) 345–358, https://doi.org/10.1016/j.mtener.2018.06.009.
[33] O. Peng, R. Shi, J. Wang, X. Zhang, J. Miao, L. Zhang, Y. Fu, P. Madhusudan, K. Liu, A. Amini, C. Cheng, Hierarchical heterostructured nickle foam–supported Co3S4 nanorod arrays embellished with edge-exposed MoS2 nanoflakes for enhanced alkaline hydrogen evolution reaction, Mater. Today Energy 18 (2020), 100513, https://doi.org/10.1016/j.mtener.2020.100513.
[34] S.L. Zhang, Y.B. Shang, C.X. Li, C.J. Li, Vacuum cold sprayed nanostructured La0.6Sr0.4Co0.2Fe0.8O3−δ as a high-performance cathode for porous metal-supported solid oxide fuel cells operating below 600 °C, Mater. Today Energy 21 (2021), 100815, https://doi.org/10.1016/j.mtener.2021.100815.
[35] O. Omoregbe, H.T. Danh, C. Nguyen-Huy, H.D. Setiabudi, S.Z. Abidin, Q.D. Truong, D.V.N. Vo, Syngas production from methane dry reforming over Ni/SBA-15 catalyst: effect of operating parameters, Int. J. Hydrogen Energy 42 (2017) 11283–11294, https://doi.org/10.1016/j.ijhydene.2017.03.146.
[36] C.N.R. Rao, S. Dey, Solar thermochemical splitting of water to generate hydrogen, Proc. Natl. Acad. Sci. U. S. A. 114 (2017) 13385–13393, https://doi.org/10.1073/pnas.1700104114.
[37] S.J. Heo, M. Sanders, R. O'Hayre, A. Zakutayev, Double-Site substitution of Ce into (Ba, Sr)MnO3Perovskites for solar thermochemical hydrogen production, ACS Energy Lett. 6 (2021) 3037–3043, https://doi.org/10.1021/acsenergylett.1c01214.
[38] S. Dey, B.S. Naidu, C.N.R. Rao, Ln0.5A0.5MnO3 (Ln=Lanthanide, A= Ca, Sr) perovskites exhibiting remarkable performance in the thermochemical generation of CO and H2 from CO2 and H2O, Chem. Eur. J. 21 (2015) 7077–7081, https://doi.org/10.1002/chem.201500442.
[39] H. Kaneko, T. Miura, H. Ishihara, S. Taku, T. Yokoyama, H. Nakajima, Y. Tamaura, Reactive ceramics of CeO2-MOx (M=Mn, Fe, Ni, Cu) for H2 generation by two-step water splitting using concentrated solar thermal energy, Energy 32 (2007) 656–663, https://doi.org/10.1016/j.energy.2006.05.002.
[40] G. Luciani, G. Landi, A. Aronne, A. Di Benedetto, Partial substitution of B cation in La0.6Sr0.4MnO3 perovskites: a promising strategy to improve the redox properties useful for solar thermochemical water and carbon dioxide splitting, Sol. Energy 171 (2018) 1–7, https://doi.org/10.1016/j.solener.2018.06.058.
[41] A.E. Ramos, D. Maiti, Y.A. Daza, J.N. Kuhn, V.R. Bhethanabotla, Co, Fe, and Mn in La-perovskite oxides for low temperature thermochemical CO2 conversion, Catal. Today 338 (2019) 52–59, https://doi.org/10.1016/j.cattod.2019.04.028.
[42] B. Xu, Y. Bhawe, M.E. Davis, Spinel metal oxide-alkali carbonate-based, low-temperature thermochemical cycles for water splitting and CO2 reduction, Chem. Mater. 25 (2013) 1564–1571, https://doi.org/10.1021/cm3038747.
[43] S. Sam, et al., Preparation of MnFe2O4 nanoceramic particles by soft chemical routes, Int. J. Appl. Sci. Eng. 9 (2011) 223–239.
[44] A. Vedrtnam, K. Kalauni, S. Dubey, A. Kumar, A comprehensive study on structure, properties, synthesis and characterization of ferrites, AIMS Mater. Sci. 7 (2020) 800–835, https://doi.org/10.3934/matersci.2020.6.800.
[45] S. Gyergyek, D. Makovec, A. Kodre, I. Arčon, M. Jagodič, M. Drofenik, Influence of synthesis method on structural and magnetic properties of cobalt ferrite nanoparticles, J. Nanoparticle Res. 12 (2010) 1263–1273, https://doi.org/10.1007/s11051-009-9833-5.
[46] H.M. Rietveld, A profile refinement method for nuclear and magnetic structures, J. Appl. Crystallogr. 2 (1969) 65–71, https://doi.org/10.1107/s0021889869006558.
[47] L. Lutterotti, S. Matthies, H.-R. Wenk, MAUD: a friendly Java program for material analysis using diffraction, IUCr Newsl. CPD. 21 (1999) 14–15.
[48] C. Dong, X. Liu, H. Guan, X. Xiao, Y. Wang, Combustion synthesized hierarchically porous Mn3O4 for catalytic degradation of methyl orange, Can. J. Chem. Eng. 95 (2017) 643–647, https://doi.org/10.1002/cjce.22723.
[49] K. Edström, S. Ito, R.G. Delaplane, Crystal and magnetic structure of non-stoichiometric K+β-ferrite, J. Magn. Magn Mater. 212 (2000) 347–354, https://doi.org/10.1016/S0304-8853(99)00831-8.
[50] J.P. Boilot, P. Colomban, G. Collin, R. Comes, Crystal structure and ion-ion correlation in ion-rich β alumina type compounds. II. potassium β ferrite, Solid State Ionics 1 (1980) 69–76, https://doi.org/10.1016/0167-2738(80)90023-5.
[51] A. Mao, H.Z. Xiang, Z.G. Zhang, K. Kuramoto, H. Zhang, Y. Jia, A new class of spinel high-entropy oxides with controllable magnetic properties, J. Magn. Magn Mater. 497 (2020), 165884, https://doi.org/10.1016/j.jmmm.2019.165884.
[52] R. Arulmurugan, B. Jeyadevan, G. Vaidyanathan, S. Sendhilnathan, Effect of zinc substitution on Co-Zn and Mn-Zn ferrite nanoparticles prepared by co-precipitation, J. Magn. Magn Mater. 288 (2005) 470–477, https://doi.org/10.1016/j.jmmm.2004.09.138.
[53] G. Jagadish Kumar, A. Banerjee, A.S.K. Sinha, Y. Su, K. Nemkovski, C. Rath, Cation distribution and magnetic properties of Zn-substituted CoCr2O4 nanoparticles, J. Appl. Phys. 123 (2018), 223905, https://doi.org/10.1063/1.5027137.